Spectrochimica Acta Part A 81 (2011) 529–543

Contents lists available at ScienceDirect

Spectrochimica Acta Part A: Molecular and Biomolecular Spectroscopy

journal homepage: www.elsevier.com/locate/saa

Structural and *in vitro* cytotoxicity studies on 1H-benzimidazol-2-ylmethyl-N-phenyl amine and its Pd(II) and Pt(II) complexes

Nour T. Abdel Ghani, Ahmed M. Mansour*

Chemistry Department, Faculty of Science, Cairo University, Gamaa Street, Giza 12613, Egypt

ARTICLE INFO

Article history:
Received 28 April 2011
Received in revised form 16 June 2011
Accepted 19 June 2011

Keywords:
Benzimidazole
Biological studies
DFT
NBO
Thermal

ABSTRACT

$[MLCl_2]\cdot zH_2O$ (L = (1H-benzimidazol-2-ylmethyl)-N-phenyl amine; M = Pd, $z = 0$; M = Pt, $z = 1$) and $[PdL(OH_2)_2]\cdot 2X\cdot zH_2O$ (X = Br, I, NO_3, $z = 0$; X = SCN, $z = 1$) complexes were synthesized as potential anticancer compounds and characterized by elemental analysis, spectral and thermal methods. FT-IR and ^{1}H NMR studies revealed that the benzimidazole L is coordinated to the metal ions *via* the pyridine-type nitrogen (N_{py}) of the benzimidazole ring and secondary amino group (NH_{sec}). Quantum mechanical calculations of energies, geometries, vibrational wavenumbers, and ^{1}H NMR of the benzimidazole L and its complexes were carried out by density functional theory using B3LYP functional combined with 6-31G(d) and LANL2DZ basis sets. Natural bond orbitals (NBOs) and frontier molecular orbitals were performed at B3LYP/LANL2DZ level of theory. The synthesized ligand, in comparison to its metal complexes was screened for its antibacterial activity. The benzimidazole L is more toxic against the bacterium *Staphylococcus aureus* (MIC = 58 μg/mL) than the standard *tetracycline* (MIC = 82 μg/mL). The complexes showed cytotoxicity against *breast cancer*, *Colon Carcinoma*, and *human heptacellular Carcinoma* cells. The platinum complex (**6**) displays cytotoxicity (IC_{50} = 12.4 μM) against *breast cancer* compared with that reported for cis-platin 9.91 μM.

1. Introduction

The great success of cis-platin as an antitumor drug has attracted considerable attention in the search for new anticancer platinum and other metal complexes with better pharmacological properties [1]. Among the non-platinum compounds with potential for the clinical treatment of human malignancies, palladium derivatives have received considerable interest, because of the structural analogy between the Pt(II) and Pd(II) complexes. The design of Pd(II) compounds with anticancer activity represents an exciting task, since Pd(II) compounds exchange ligands 105 times faster than analogous Pt(II) compounds [2]. Due to this rapid exchange, Pd(II) derivatives do not maintain their structural integrity long enough to reach the pharmacological target. To overcome their high lability, chelating ligands have been used to afford high thermodynamic stabile and kinetically inert Pd(II) complexes [2]. Recently, interest has been directed towards developing of cis-platin analogs with heterocyclic amine ligands [3], e.g. benzimidazole. The benzimidazole scaffold is a useful structural motif for displaying chemical functionality in biologically active molecules. Some of its derivatives have potent biological activities as antitumor, anti-HIV, and antimicrobial agents [4]. At the same time, owing to the coordination ability of azoles, the chelating ligands incorporating benzimidazole groups have been extensively studied in the context of modeling biological systems in recent years [5]. Thus, a considerable number of metal benzimidazole complexes including most transition metals were studied as reported by Linert et al. [6].

Our aim was to take into account all the previously mentioned properties of anticancer drugs and synthesize Pt(II) and Pd(II) complexes of the benzimidazole ligand (L) (Fig. 1) that could be proved to be potent antitumor agents. The structures of L and its complexes were elucidated by elemental analysis, FT-IR, ^{1}H NMR, MS, UV/vis, X-ray powder diffraction, and thermal analysis. Quantum mechanical calculations of energies, geometries, vibrational wavenumbers, and ^{1}H NMR of the benzimidazole L and its complexes were carried out by using *density functional theory* (DFT). Natural bond orbital (NBO) analysis was performed to provide details about the type of hybridization and the nature of bonding in the complexes.

2. Experimental

2.1. Synthesis of the ligand (L) and its complexes

All chemicals used in the preparation and investigation of the present study were of reagent grade (Sigma). The benzimidazole L was prepared by condensation of equimolar quantities of 2-chloromethylbenzimidazole [7] with aniline in ethanol in the presence of small amount of sodium iodide for about 18–24 h. At

* Corresponding author. Tel.: +20 2 0122211253; fax: +20 2 35728843.
E-mail address: inorganic_am@yahoo.com (A.M. Mansour).

1386-1425/$ – see front matter © 2011 Elsevier B.V. All rights reserved.
doi:10.1016/j.saa.2011.06.046

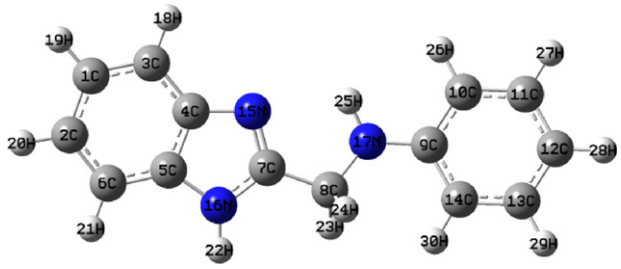

Fig. 1. The optimized structure of benzimidazole ligand (L).

the end of the reaction period, the mixture was neutralized and the solid was separated by dilution with de-ionized water, and re-crystallized from benzene/petroleum ether.

The solid Pd(II) (**1**), and Pt(II) (**6**) metal chlorides (X = Cl) complexes were prepared by adding a hot ethanolic solution (60 °C) of the ligand L (1 mmol) to a hot aqueous solution (60 °C) of the metal ions (1 mmol; K_2PdCl_4, or K_2PtCl_4). The resulting mixtures were stirred under reflux for about 1–2 h, whereupon the complexes were precipitated. The palladium complexes with other anions (X = Br, I, SCN and NO_3) (**2**–**5**) were synthesized by adding 0.664 g KI, 0.408 g NaBr, 0.304 g NH_4SCN, or 0.404 g KNO_3 to 1 mM K_2PdCl_4 solution. Then, 1 mM of the hot ethanolic solution of the ligand L was added. The results of elemental analyses are in a good agreement with those calculated for the suggested formula and the melting point is sharp indicating the purity of the prepared benzimidazole ligand. The molar conductance values of Pd-L (X = Cl) (**1**) and Pt-L (**6**) complexes in DMF indicate the non-electrolytic nature of these complexes, while the higher conductance values of the other complexes suggest their ionic nature.

- Data for **L** ($C_{14}H_{13}N_3$). Color: Orange-Yellow. Yield: 75%. MS: M^+ = 223 (calcd. 223.27). Anal. Calc. %C, 75.25; %H, 5.82; %N, 18.81. Found: %C, 75.65%; %H, 5.72; %N, 18.73. FT-IR: 3427 (ν(NH)$_{sec}$), 3052 (ν CH^{ass}/An), 2889 (ν CH$_2{}^{ass}$), 2830 (ν CH$_2{}^{ss}$), 1687 ν(C=N), 1599 (ν CC^{ss}/An), 1421 ν(C–N)$_{Bz}$, and 1309 cm^{-1} ν(C–N)$_{sec}$. ^{1}H NMR (DMSO): δ 12.20 (1H, s, benzimidazolic NH); 6.55 (2H), 6.65 (1H), and 7.05 (2H) (aniline protons, H$^{26-30}$); 7.10, 7.12, 7.47, and 7.49 (benzimidazolic protons, H$^{18-21}$); δ 6.23 (1H, t, NH$_{sec}$), and δ 4.46 (2H, d, CH$_2$). UV/vis (ethanol): 204, 222, 242, 274, and 280 nm; (DMF): 263, 275, and 281 nm.
- Data for **Pd-L** (**X = Cl**) (**1**) ($C_{14}H_{15}Cl_2N_3OPd$). Color: Yellow. Yield: 80%. Anal. Calc. %C, 40.17; %H, 3.61; %Cl, 16.94; %N, 10.04; %Pd, 25.42. Found: %C, 40.39; %H, 3.82; %Cl, 16.99, %N, 10.13; %Pd, 25.44. FT-IR: 3399 (ν(NH)$_{sec}$), 1614 (ν(C=N)), 1444 (ν(NH$_b$)$_{sec}$), 1281 (ν(C–N)$_{sec}$), and 510 ρ_t(OH$_2$). ^{1}H NMR (DMSO): δ 13.18 (NH$_{Bz}$), δ 6.56–8.48 (9H, aromatic protons), δ 7.46 (NH$_{sec}$) and δ 4.98 and 5.31 (CH$_2$). UV/vis (DMF): 272, 278, and 372 nm. Molar Cond. (10^{-3}, DMF): 21.11 Ω^{-1} cm^2 mol^{-1}.
- Data for **Pd-L** (**X = Br**) (**2**) ($C_{14}H_{17}Br_2N_3O_2Pd$). Color: Orange. Yield: 85%. Anal. Calc. %C, 32.00; %H, 3.26; %Br, 30.41; %N, 8.00; %Pd, 20.25. Found: %C, 31.89; %H, 3.23; %Br, 30.38, %N, 7.92; %Pd, 20.17. FT-IR: 3431 (ν(NH)$_{sec}$), 1659 (ν(C=N)), 1443 (ν(NH$_b$)$_{sec}$), 1321 (ν(C–N)$_{Bz}$), 1281(ν(C–N)$_{sec}$) and 510 ρ_t(OH$_2$). ^{1}H NMR (DMSO): δ 13.17 (NH$_{Bz}$), δ 6.50–8.45 (9H, aromatic protons), δ 6.90 (NH$_{sec}$) and δ 5.01 and 5.26 (CH$_2$). UV/vis (DMF): 271, 281, and 362 nm. Molar Cond. (10^{-3}, DMF): 419 Ω^{-1} cm^2 mol^{-1}.
- Data for **Pd-L** (**X = I**) (**3**) ($C_{14}H_{17}I_2N_3O_2Pd$). Color: Blue-Black. Yield: 82%. Anal. Calc. %C, 27.14; %H, 2.77; %I, 40.97; %N, 6.78; %Pd, 17.18. Found: %C, 27.07; %H, 2.74; %I, 40.93, %N, 6.71; %Pd, 17.11. FT-IR: 3414 (ν(NH)$_{sec}$), 3263 (ν(NH)$_{Bz}$), 1675 (ν(C=N)), 1454 (ν(NH$_b$)$_{sec}$), 1311(ν(C–N)$_{Bz}$), 1263 (ν(C–N)$_{sec}$), 855 ρ_r(OH$_2$), 624 ρ_w(OH$_2$), and 466 ρ_t(OH$_2$). ^{1}H NMR (DMSO): δ 13.14 (NH$_{Bz}$), δ 6.60–8.32 (10H, aromatic protons + NH$_{sec}$), and δ 4.76, 5.18 (CH$_2$). UV/vis (DMF): 277, 284, and 367 nm. Molar Cond. (10^{-3}, DMF): 431 Ω^{-1} cm^2 mol^{-1}.
- Data for **Pd-L** (**X = SCN**) (**4**) ($C_{16}H_{19}N_5O_3S_2Pd$). Color: Deep yellow. Yield: 86%. Anal. Calc. %C, 37.10; %H, 4.09; %N, 13.52; %Pd, 20.55. Found: %C, 36.89; %H, 4.03; %N, 13.52; %Pd, 20.49. FT-IR: 3417 (ν(NH)$_{sec}$), 3359 (ν(NH)$_{Bz}$), 2114 ν(C≡N), 1672 (ν(C=N)), 1455 (ν(NH$_b$)$_{sec}$), 1310 (ν(C–N)$_{Bz}$), 1256 (ν(C–N)$_{sec}$), 866 ρ_r(OH$_2$), and 629 ρ_w(OH$_2$). ^{1}H NMR (DMSO): δ 13.46 (NH$_{Bz}$), δ 6.57–8.40 (9H, aromatic protons), δ 6.68 (NH$_{sec}$), and δ 4.92 and 5.14 (CH$_2$). UV/vis (DMF): 276, 282, and 348 nm. Molar Cond. (10^{-3}, DMF): 449 Ω^{-1} cm^2 mol^{-1}.
- Data for **Pd-L** (**X = NO$_3$**) (**5**) ($C_{14}H_{17}N_5O_8Pd$). Color: Grey-Green. Yield: 80%. Anal. Calc. %C, 34.33; %H, 3.50; %N, 14.30; %Pd, 21.73. Found: %C, 34.51; %H, 3.60; %N, 14.28; %Pd, 21.70. FT-IR: 3410 (ν(NH)$_{sec}$), 1657 (ν(C=N)), 1489 (ν_{ass}(NO$_2$)), 1442 (ν(NH$_b$)$_{sec}$), 1385 (ν_{ss}(NH$_b$)$_{sec}$), 1322 (ν(C–N)$_{Bz}$), 1283 (ν(C–N)$_{sec}$), 930 (ν(NO)), 838 ρ_r(OH$_2$), 624 ρ_w(OH$_2$), and 510 ρ_t(OH$_2$). ^{1}H NMR (DMSO): δ 13.21 (NH$_{Bz}$), δ 6.20–8.96 (9H, aromatic protons), δ 6.93 (NH$_{sec}$) and δ 5.18 and 5.36 (CH$_2$). UV/vis (DMF): 277, 282, and 354 nm. Molar Cond. (10^{-3}, DMF): 375 Ω^{-1} cm^2 mol^{-1}.
- Data for **Pt-L** (**X = Cl**) (**6**) ($C_{14}H_{13}Cl_2N_3Pt$). Color: Brown. Yield: 72%. Anal. Calc. %C, 34.37; %H, 2.68; %Cl, 14.49; %N, 8.59; %Pt, 39.87. Found: %C, 34.51; %H, 2.81; %Cl, 14.58, %N, 8.61; %Pt, 39.94. FT-IR: 3382 (ν(NH)$_{sec}$), 3245 (ν(NH)$_{Bz}$), 1625 (ν(C=N)), 1453 (ν(NH$_b$)$_{sec}$), and 1278 (ν(C–N)$_{sec}$). ^{1}H NMR (DMSO): δ 13.18 (NH$_{Bz}$), δ 6.56–8.48 (9H, aromatic protons), δ 7.01 (NH$_{sec}$) and δ 4.80 and 4.96 (CH$_2$). UV/vis (DMF): 274, 280, 351, and 422 nm. Molar Cond. (10^{-3}, DMF): 12.04 Ω^{-1} cm^2 mol^{-1}.

2.2. Instruments

Infrared spectra were recorded as KBr pellets using *FTIR-460 plus, JASCO*, in 4000–200 cm^{-1} region. The ^{1}H NMR spectra were run at 300 MHz in DMSO-d$_6$ using *Varian-Oxford Mercury VX-300 NMR*. The mass spectra were recorded by the aid of *SHIMADZU QP-2010 plus mass spectrometer* at 70 eV. The X-ray powder diffraction patterns were recorded over 2θ = 5–60° range using *Philips X-ray diffractometer model PW 1840*. Radiation was provided by copper anode (K_α, λ = 1.54056 Å) operated at 40 kV and 25 mA. The thermal analyses (TGA/DTA) were carried out in dynamic nitrogen atmosphere (20 mL min^{-1}) with a heating rate of 10 °C min^{-1} in platinum crucible using *DTG-60H SIMULTANEOUS DTA-TG APPARATUS-SHIMADZU*. Elemental microanalyses (C, H, N, and X) were performed at the Micro-analytical Center, Cairo University. The analyses were repeated twice to check the accuracy of the analyzed data. The metal content was determined gravimetrically [8]. Digital *Jenway 4330* Conductivity-pH meter with (1.02) cell constant was used for pH and molar conductance measurements. The UV/vis measurements were carried out using automated spectrophotometer UV/vis *SHIMADZU Lambda 4B* using 1 cm matched quartz cells.

2.3. Theoretical calculations

The molecular structure of the benzimidazole (L) in the ground state was optimized by a DFT method using B3LYP functional [9] combined with 6-31G(d) and LANL2DZ basis sets. Calculations were carried out using *GAUSSIAN 03* [10]. The vibrational frequencies and the corresponding normal modes were evaluated at the optimized geometry [9] using the same basis sets. Vibrational modes were analyzed using GAUSSVIEW software [11]. The main reason in choosing the LANL2DZ basis set is its inclusion of relativistic effect that is essential for heavy elements, e.g. Pd(II) and Pt(II), in

order to compare between the optimized structures of the ligand L and its complexes. The ^{1}H NMR chemical shifts were computed at the B3LYP/6-311+G(2d,p) level of theory in the gaseous state by applying GIAO approach [12] and the values for the ^{1}H isotropic were referenced to TMS, which was calculated at the same level of theory. The optimized structures, vibrational frequencies, ^{1}H chemical shifts, and the natural bond orbitals (NBOs) analysis of the metal complexes were obtained at B3LYP/LANL2DZ level of theory.

2.4. Biological activity

2.4.1. Antimicrobial activity

The antimicrobial activities of the test samples were determined using a modified Kirby-Bauer disc diffusion method [13] under standard conditions using *Mueller-Hinton* agar medium, as described by NCCLS [14]. The antimicrobial activities were carried out using culture of *Bacillus subtilis*, *Staphylococcus aureus*, and *Streptococcus faecalis* as Gram-positive bacteria and *Escherichia coli*, *Pseudomonas aeruginosa*, and *Neisseria gonorrhoeae* as Gram-negative bacteria. Briefly, 100 μL of the test bacteria were grown in 10 mL of fresh media until they reached a count of approximately 108 cells/mL. A 100 μL of microbial suspension was spread onto agar plates corresponding to the broth in which they were maintained. DMSO (0.1 mL) alone was used as control under the same conditions for each microorganism, subtracting the diameter of inhibition zone resulting with DMSO, from that obtained in each case. The antimicrobial activities could be calculated as a mean of three replicates. The results were compared with a similar run of *Tetracycline* as an antibacterial.

2.4.2. Cell culture and cytotoxicity determination

Three human cancer cell lines were used for *in vitro* screening experiments; *breast cancer* (MCF7), *Colon Carcinoma* (HCT) and *human heptacellular Carcinoma* (Hep-G2). They were obtained frozen in liquid nitrogen (−180 °C) from the American Type Culture Collection. The tumor cell lines were maintained in the National Cancer Institute, Cairo, Egypt, by serial sub-culturing. Cell culture cytotoxicity assays were carried out as described previously [15]. RPMI-1640 medium was used for culturing and maintenance of the human tumor cell lines [15]. Cells were seeded in 96-well plates at a concentration of 5×10^4 to 10^5 cell/well in a fresh medium and left to attach to the plates for 24 h. Growth inhibition of cells was calculated spectrophotometrically using a standard method with the protein-binding dye sulforhodamine B (SRB) [16]. The results were compared with a similar run of cis-platin as an antitumor compound.

3. Result and discussion

3.1. IR spectral studies

The theoretical IR spectra of the benzimidazole (L) were obtained at DFT/B3LYP level of theory using 6-31G(d) and LANL2DZ basis sets. All band assignments are presented in Table 1. At this level, the calculated harmonic force constants and frequencies are higher than the corresponding experimental quantities, due to basis set truncation, neglecting of electron correlation and mechanical anharmonicity [17]. To compensate these shortcomings, scale factors were introduced and an explanation of this approach was discussed [18]. Two different methods were applied: (i) *uniform* scaling [18], the scaling factors are 0.963 for 6-31G(d) and 0.970 for LANL2DZ basis sets, (ii) *linear regression method* [19], in this method, the plot of the calculated frequencies versus their experimental values resulted in a straight line, whose equation was used to correct the calculated frequencies (ν_{calc}).

Benzimidazole ligand (L) has a strong intermolecular hydrogen bond in the solid state, which makes the IR spectrum shows strong and broad absorption band in the region 3500–2200 cm^{-1}. Thus, it is difficult to assign the benzimidazolic NH band (NH_{Bz}) experimentally (Fig. 2). By using the B3LYP/6-31G(d) method, the scaled calculated value at 3513 cm^{-1} is assigned to the $\nu(NH_{Bz})$. This group is still masked in the spectra of metal complexes, due to the hydrogen bond effect generated by water molecules, whereas complexes (**3**,**4**) have a sharp band at 3263 and 3359 cm^{-1}, respectively [3]. The theoretically scaled $\nu(NH_{Bz})$ in the benzimidazole (L) and its complexes is found in the same position at 3570 cm^{-1} as calculated by the LANL2DZ basis set. This confirms that the NH_{Bz} group remains intact in the complexes.

The sharp band at 3427 cm^{-1} in the benzimidazole L is assigned to $\nu(NH_{sec})$ that is in a good agreement with the theoretically scaled value. This band is still observed in the complexes, but it shifts to lower frequency and/or becomes broad (3431–3382 cm^{-1}), indicating its involvement in the coordination sphere. The scaled $\nu(NH_{sec})$ is found at 3502, 3374, and 3353 cm^{-1} in the benzimidazole L, Pd-L (**1**) and Pt-L (**6**) complexes, respectively. This confirms the participation of this group in the coordination sphere. The stretching mode of the C=N group is observed at 1682 cm^{-1} in the free ligand (theoretical value is 1683 cm^{-1}) and is shifted to lower frequencies by 12–63 cm^{-1} in its complexes. This confirms the participation of the pyridine-type nitrogen in the coordination sphere. Other vibration modes are shown in Table 1.

Unfortunately, the metal-nitrogen stretching bands could not be distinguished experimentally from other ring skeleton vibrations present in the same region [3]. However, the theoretically scaled vibrations at 290 and 264 cm^{-1} in the Pd-L complex (**1**) are assigned to Pd-N_{py} and Pd-NH_{sec}, while the bands at 271 and 216 cm^{-1} are allocated for Pt-N_{py} and Pt-NH_{sec} in the Pt-L complex (**6**). The far-IR spectra of the palladium complexes (**1**–**3**) (X = Cl, Br or I) show two medium bands only in case of X = Cl at 367 and 363 cm^{-1} due to ν(Pd–Cl) in a cis-square planar structure [19]. Similarly, the platinum complex (**6**) shows these modes at 369 and 360 cm^{-1}. In addition, the theoretical assignments of these bands are easily assigned by the visualization of the normal mode displacement vectors utilizing the *GAUSSVIEW* program. The theoretically scaled ν_{ss}(Pd–Cl) and ν_{ass}(Pd–Cl) modes are observed at 330 and 320 cm^{-1}, while the scissoring bending mode of Cl–Pd–Cl is found at 128 cm^{-1}. For platinum complex (**6**), the theoretically scaled ν_{ss}(Pt–Cl), ν_{ass}(Pt–Cl) and the scissoring Cl–Pt–Cl modes are established at 322, 316 and 136 cm^{-1}, respectively.

The IR spectrum of the palladium thiocyanato complex (**4**) displays ν(C≡N) as strong band at 2114 cm^{-1}. This value is higher than that found in case of N-bonded and S-bonded complexes [20], which indicates that the thiocyanate anions are out of the coordination sphere as suggested from the conductivity measurements. The disappearance of M–N or M–S stretching modes confirms the absence of SCN in the coordination sphere. Similarly, the nitrato complex (**5**) shows three bands at 1489, 1385 and 930 cm^{-1} owing to the $\nu(NO_2)_{asy}$, $\nu(NO_2)_{sy}$ and ν(NO) [20]. The IR spectra of complexes (**2**–**5**) showed a very broad band centered at 3400 cm^{-1} associated by librational modes of water [20]. For example, the nitrato complex (**5**) exhibits the librational modes (rocking (ρ_r), twisting (ρ_t) and wagging (ρ_w)) at 838, 624 and 510 cm^{-1}, respectively.

The RMS error of the frequencies between the un-scaled and experimentally observed values in the benzimidazole L was found to be 79.3 cm^{-1}. After scaling, the RMS error are found to be 5.2 and 23.3 cm^{-1} for 6-31G(d) and LANL2DZ, respectively, suggesting that the 6-31G(d) basis set gives more accurate results. Finally, IR study reveals that the ligand coordinated to the metal ions *via* the pyridine-type nitrogen (N_{py}) of the benzimidazole ring and secondary amino group (NH_{sec}).

Table 1
Band assignment of experimental and theoretical IR spectra of benzimidazole (L).

No.	Exp. freq.	Calculated un-scaled frequency *B3LYP*		Scaled frequency *Uniform scaling*		Scaled frequency *Linear regression scaling*		Vibrational assignments
		6-31G(d)	LANL2DZ	6-31G(d)	LANL2DZ	6-31G(d)	LANL2DZ	
1		3649	3681	3513	3570	3516	3516	ν NH^{ss}/Bz
2	3427	3563	3611	3431	3502	3433	3450	ν NH^{ss}/An
3		3219	3238	3099	3140	3101	3093	ν CH^{ss}/Bz
4		3211	3229	3092	3132	3093	3084	ν CH^{ss}/An
5		3209	3224	3090	3127	3092	3080.	ν CH^{ass}/Bz
6		3203	3212	3084	3115	3086	3068	ν CH^{ass}/An
7		3197	3209	3078	3112	3080	3065	ν CH^{ass}/Bz
8		3191	3202	3072	3105	3074	3059	ν CH^{ass}/An
9		3187	3196	3069	3100	3070	3053	ν CH^{ass}/Bz
10		3180	3186	3062	3090	3064	3043	ν CH^{ass}/An
11	3052	3173	3180	3055	3084	3057	3038	ν CH^{ass}/An
12	2889	2999	2984	2888	2894	2889	2850	$CH_2{}^{ass}$
13	2830	2942	2963	2833	2874	2834	2830	$CH_2{}^{ss}$
14	1687	1683	1675	1620	1624	1621	1599	ν CC/Bz + ν C=N/Bz + β NH^{sc}/Bz
15	1599	1672	1664	1610	1614	1610	1589	ν CC/An
16		1643		1582		1582		ν CC/Bz + ν CC/An + β NH/Bz + β NH/An
		1641		1580		1580		
17			1635		1585		1561	ν CC/Bz + β NH/Bz
18			1628		1579		1554	ν CC/An + β NH^{sc}/An
19		1595	1582	1535	1534	1536	1510	ν CC/Bz + β NH/Bz + β NH/An + $\delta_s CH_2$ + ν C=N/Bz
20	1505	1564	1555	1506	1508	1506	1485	ν CC/An + β NH/An + $\delta_s CH_2$
		1550		1492		1493	1466	
21		1543		1485		1486		$\delta_s CH_2$
22		1535		1478		1478		ν CC/Bz + $\delta_s CH_2$
23			1535		1489		1413	δ_s CH_2 + β NH/An
24		1497	1480	1441		1441		ν CC/Bz (boat shape) + ω CH_2
25	1421	1493	1528	1437	1482	1438	1459	ν CC/An + β NH/An + ω CH_2
26	1339		1513		1467		1445	ν CC/Bz + ν C=N/Bz + ω CH_2
27			1477		1432		1410	ν CC/An + β NH/An + ω CH_2
28		1460	1437	1405	1394	1406	1372	ν C–NH/An + β NH/An + β NH/An + ω CH_2
			1431		1388		1366	
29		1377	1390	1326	1348	1326	1327	ν CC/An + β CH/An
30			1372		1331		1310	β CH/An
31		1370		1319		1319		β CH/An + β CH/Bz + ω CH_2 + β NH/Bz
32	1309	1365	1365	1314	1324	1314	1303	β CH/An + C–N/An + ω CH_2
33	1266	1332		1282		1282		β CH/An + β CH/Bz
34			1326		1286		1266	β CH/An + β CH/Bz + β NH/An
35		1306		1257		1257		ν CC/Bz + β NH/An
36			1302		1263		1243	β CH/An + β CH/Bz + β NH/An + β NH/Bz + ω CH_2
37		1295	1290	1247	1251	1247	1231	ν CC/Bz + ω CH_2 + β NH/An
38		1259		1212		1212		τ CH_2 + β NH/Bz + β CH/Bz
39		1247	1250	1200	1213	1200	1193	τCH_2
40			1247		1209		1190	β CH/Bz + β NH/Bz
41			1227		1190		1171	β CH/An + β CH/Bz + β NH/Bz + ω CH_2
42	1186	1217	1220	1171	1183	1172	1165	β CH^{sc}/An
43		1206		1161		1161		β NH/Bz + β CH/An + β CH/Bz
44		1191	1202	1146	1166	1146	1147	β CH^{sc}/An
45		1183	1193	1139	1157	1139	1139	β CH^{sc}/Bz
46		1161	1162	1118	1127	1118	1109	ν CH/An + CH_2-NH + β NH/Bz
47	1107	1144	1140	1101	1105	1101	1088	β CH^{sc}/Bz
48		1112	1107	1070	1073	1070	1057	β CH/An
49	1016	1058		1018		1018		β CH/An
50		1046		1007		1007		β CH/Bz
51		1040	1050	1001	1018	1001	1002	ρCH_2
		674	675	649	654	648	644	
52		1023	1046	985	1014	985	998	Rtorsion/Bz
53		1008	1035	970	1004	970	988	Rtrigd/An
		975	1020	938	989	938	973	
	841	947	998	911	968	911	952	
54	745	874	910	841	882	841	868	γ
	687	822	848	791	822	791	809	CH/An
		762	785	733	761	733	749	
		705	716	678	694	678	683	
		974	1024	937	993	937	977	
		930	982	895	952	895	937	γ
55		862	896	830	869	830	855	CH/Bz
		757	786	728	762	728	750	

Table 1 (*Continued*)

No.	Exp. freq.	Calculated un-scaled frequency *B3LYP*		Scaled frequency *Uniform scaling*		Scaled frequency *Linear regression scaling*		Vibrational assignments
		6-31G(d)	LANL2DZ	6-31G(d)	LANL2DZ	6-31G(d)	LANL2DZ	
56	871	912	1009	878	978	878	963	Rtrigd/Bz
57			1004		973		958	Rtrigd/An
58			909		881		867	Rtrigd/Bz
59		634	635	610	651	610	605	Rtrigd/An
60		633		609		609		Rtrigd/Bz
		614		591		590		
61	545	579	538	557	521	557	513	NH/An
		486		468		467		
62	445	435	604	418	585	402	576	NH/Bz

For 6-31G(d) basis set, the slope is equal 1.0384 and the linear coefficient is 0.9993.
For LANL2DZ basis set, the slope is equal 1.0464 and the linear coefficient is 0.9963.
R: ring; ss: symmetric stretching; ass: asymmetric stretching; ν, stretching; β, in-plane bending; γ, out-of-plane bending; ρ, rocking; ω, wagging; τ, torsion; trig: trigonal; trigd: trigonal deformation.

3.2. ^{1}H NMR studies

1. The NH_{Bz} signal appears at 12.20 ppm [21] in the benzimidazole L and moves downfield in its complexes (13.14–13.46 ppm). This shift is related to the charge density change in the benzimidazole ring, which supports the fact that the coordination occurs *via* the pyridine-type nitrogen.
2. The triplet signal at 6.23 ppm is due to the NH_{sec} group (Fig. 3), whereas the doublet signal at 4.46 ppm is assigned to the CH_2 group. In complexes, both signals move downfield owing to the participation of the NH_{sec} group in the chelation. The methylene group appears as a pair of quartet between 4.76 and 5.36 ppm in the complexes, as the CH_2 protons are no longer isochronous, where the equatorial proton points away from the metal ion than the axial one does [7].
3. The protons of the aniline ring give rise to two doublets at 6.55, 7.05 ppm, and a singlet at 6.65 ppm. While, the four broader signals at 7.10, 7.12, 7.47, and 7.49 are attributed to the aromatic protons of the benzimidazole ring. In complexes, the aromatic protons nearest to the coordination centers are found to suffer maximum downfield shifts compared with the other aromatic protons.

The calculated chemical shift of the methylene group (4.46 ppm) in the benzimidazole (L) by the 6-311+G(2d,p) basis set is in agreement with the experimental value. The theoretical values at 7.53, 7.40, 7.10, 7.08, and 6.51 ppm are assigned to the aromatic protons of the aniline moiety, while the signals at 8.14, 7.59, 7.58, and 7.63 ppm are attributed to the benzimidazolic protons. Thus, the experimental chemical shifts are slightly smaller than the calculated values. In addition, the experimental chemical shift of NH_{Bz} proton is shifted towards higher magnetic field than the calculated ones by 4.05 ppm, as previously reported by other authors [22]. In addition, the calculated chemical shift of NH_{sec} group is smaller than that observed by 0.76 ppm. These may be due to neglect of the non-specific solute–solvent interactions (in the gas phase), and

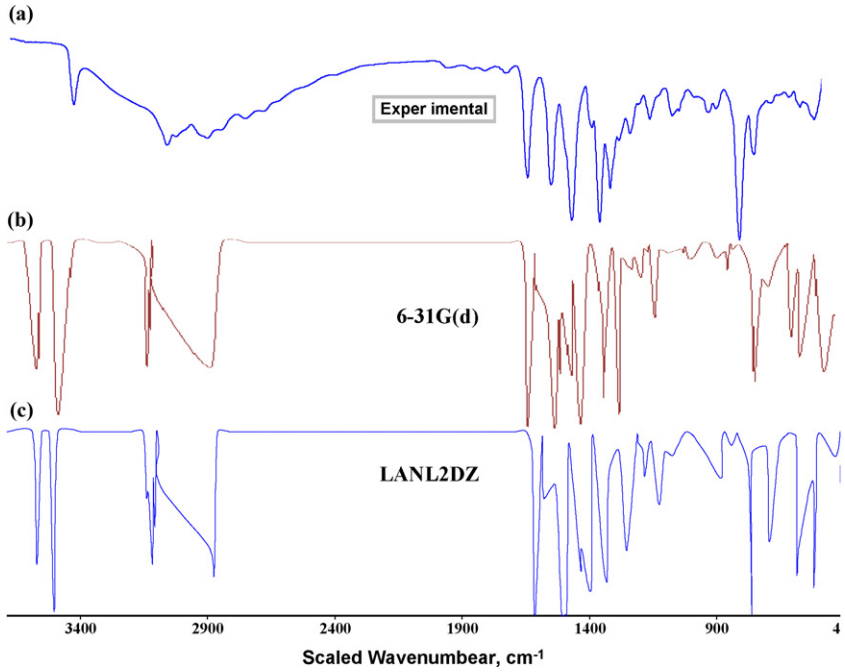

Fig. 2. Infrared spectra of benzimidazole L (a) experimental, (b) 6-31G(d), (c) LANL2DZ.

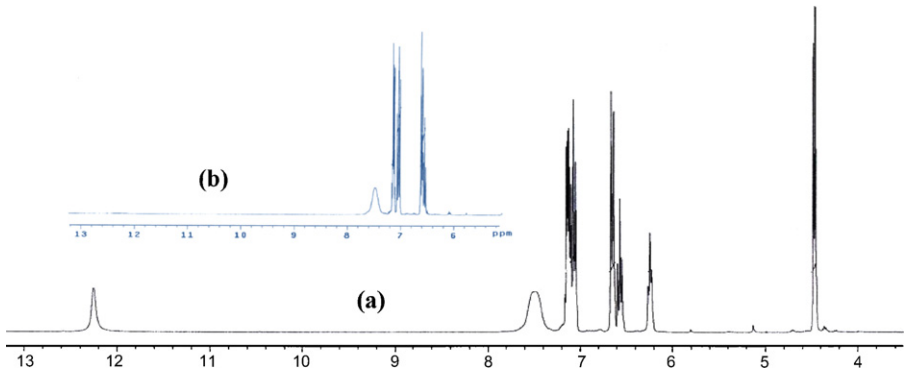

Fig. 3. ^{1}H NMR spectrum of benzimidazole L in (a) DMSO, (b) DMSO/D_2O.

the intermolecular hydrogen bond in our calculations as compared with the experimental chemical shifts that are obtained from the DMSO solutions (hydrogen-bonded solvent).

3.3. Mass spectrometry

The benzimidazole L has a molecular ion peak at m/z 223, and decomposes through the cleavage of the CH_2–NH bond. The most abundant fragment at m/z 131 is assigned to 2-methylene benzimidazole, while the fragment at m/z 93 is due to the aniline moiety. The mass spectrum of the Pd-L complex (**1**) was characterized by the appearance of the most abundant fragment at m/z 365 owing to the removal of one chlorine atom from $[PdLCl_2]^+$. The latter fragment loses the NH_{Bz} group to give a peak at m/z 350. Fragments due to 2-methylene benzimidazole, benzimidazole, and N-methylene aniline are also observed.

Fragmentation pattern of the Pt-L complex (**6**) goes under three complicated fragmentation routes as demonstrate in Scheme 1. It was found that the participation of $C{=}N_{py}$ in the chelation introduces a second weakness point through which the benzimidazole ring decomposes to imidazole moiety with the appearance of a fragment at m/z 365. The peak at m/z 417 is assigned to $[PtL]^{2+}$ fragment. This fragment confirms the bidentate nature of the benzimidazole ligand. The fragment at m/z 382 indicates the presence of two chlorine atoms in the coordination sphere of Pt-L complex.

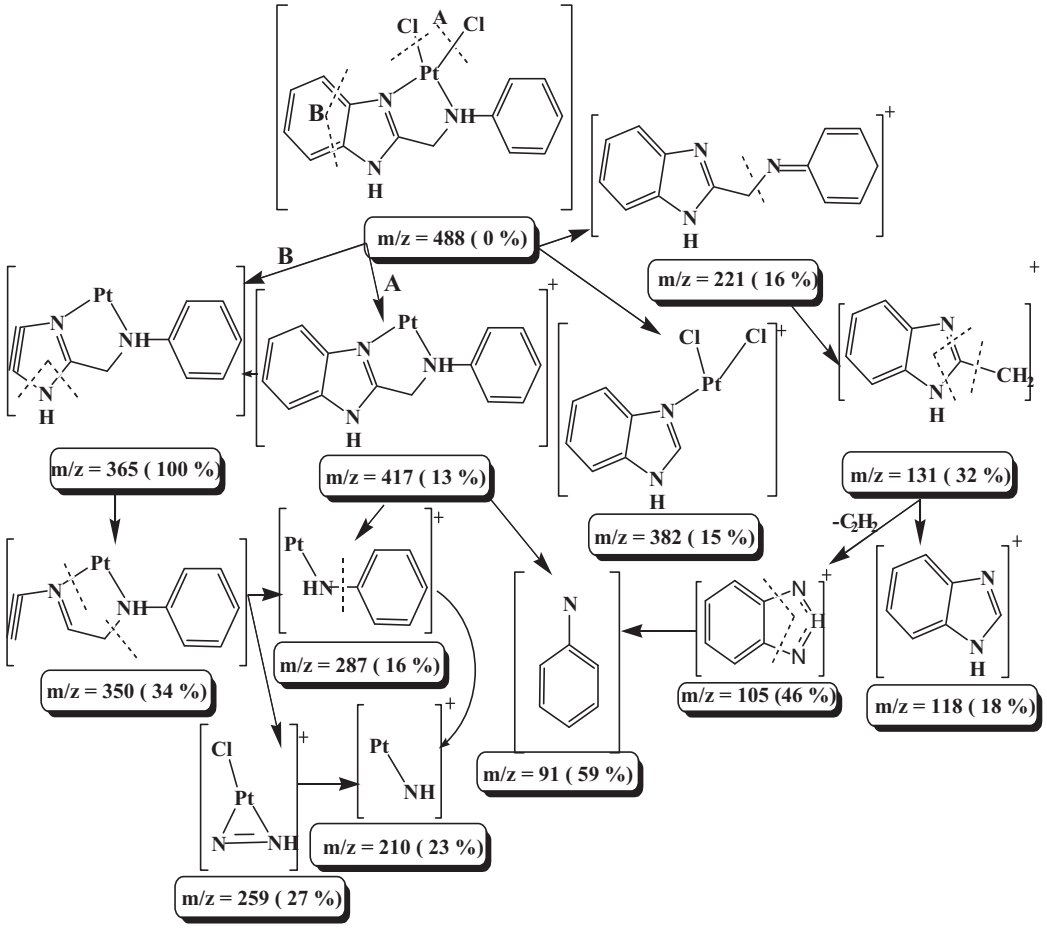

Scheme 1. Fragmentation pattern of Pt-L (**6**) complex.

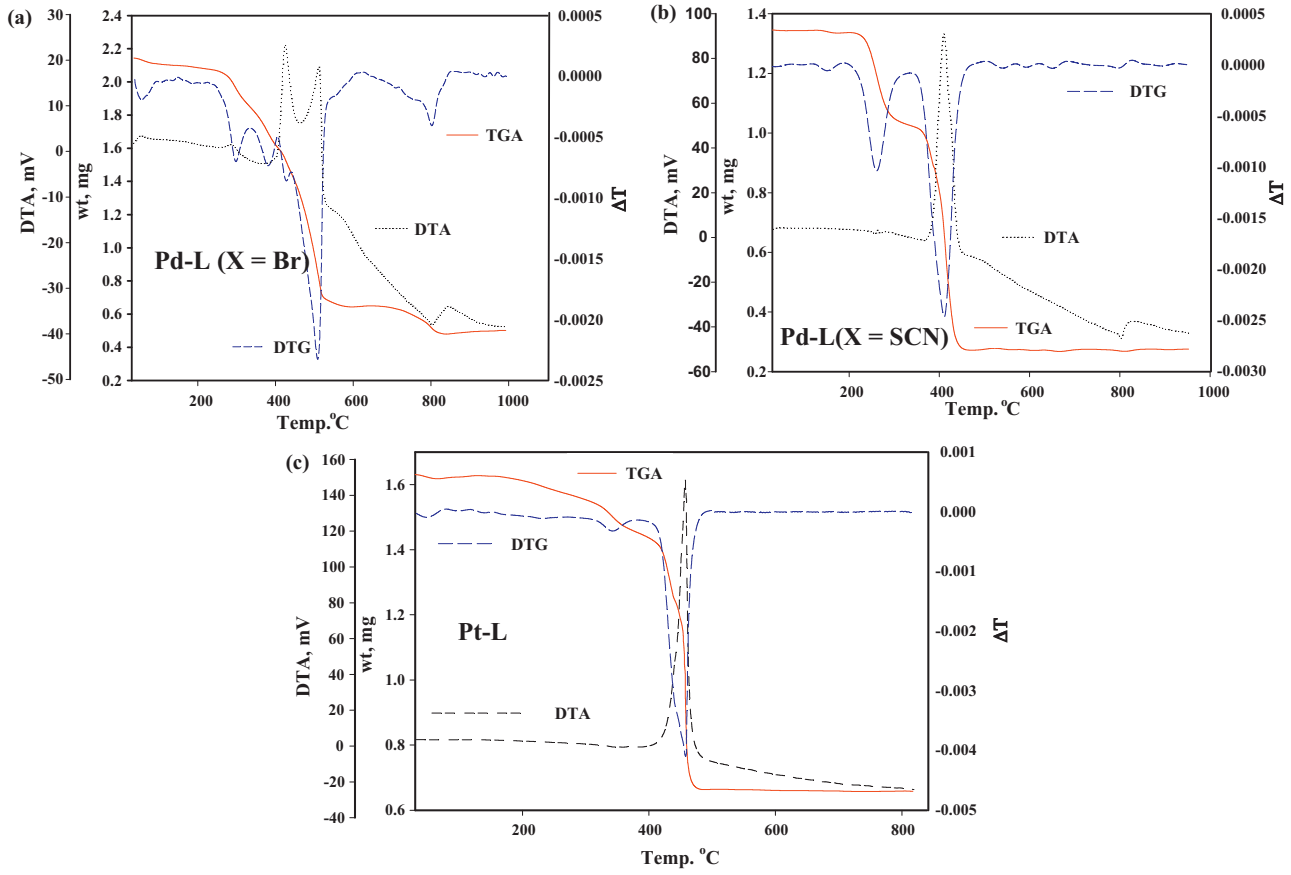

Fig. 4. TGA, DTG and DTA curves of (a) Pd-L (X = Br), (b) Pd-L (X = SCN), (c) Pt-L.

3.4. Electronic absorption

The electronic spectrum of the benzimidazole L displayed five absorption bands in ethanol at 204, 222, 242, 274 and 280 nm. The first two bands may be assigned to medium and low energy π–π^* transitions within the phenyl rings of the aniline and benzimidazole moieties, respectively [23]. The remaining bands at 242, 274 and 280 nm are assigned to π–π^* transitions in the benzimidazole ring [24]. In addition, the bands at 274 and 280 nm appear doubled as benzoic acid due to the existence of a tautomeric structure [25]. This phenomenon is supported by comparing our spectrum with the spectrum of 1-methyl-2-phenyl-benzimidazole [24], where this fine structure is lost.

The two bands between 270 and 280 nm (35,714–37,000 cm^{-1}) in the Pd(II) and Pt(II) complexes are assigned to internal ligand transitions (π–π^* in the benzimidazole ring). The band near 26,000 cm^{-1} in Pd-L (**1**) is spin-allowed transition; $a_{1g}(d_{x^2-y^2}) - b_{1g}(d_{x^2-y^2})$ i.e. $^1A_{1g} \rightarrow {}^1B_{1g}$ (ν_2). The first low energy spin allowed band at 23,696 cm^{-1} in Pt-L complex (**6**) has been assigned to the transition $b_{2g}(d_{xy}) - d_{1g}(d_{x^2-y^2})$ i.e. $^1A_{1g} \rightarrow {}^1A_{2g}$ (ν_1), comparable to the transition assigned by Jorgensen [31], for $[PtCl_4]^{2-}$ (21,500 cm^{-1}). This blue shift is ascribed to the stereochemical difference between the L and the chloride ion. Strong charge-transfer transitions may interfere and prevent observation of all the expected bands [26]. Strong bands between 350 and 380 nm (28,000–26,000 cm^{-1}) in the palladium complexes (**2**–**5**) are assignable to a combination of MLCT and $e_g(d_{yz}, d_{zx}) - b_{1g}(d_{x^2-y^2})$, i.e. $^1A_{1g} \rightarrow {}^1E_g$ bands (ν_3). Therefore, the electronic spectra of Pd(II) and Pt(II) metal complexes are indicative of square planar geometry [26,27].

3.5. Thermal analyses and kinetics studies

Discussing the simultaneous TGA/DTA curves constructed for Pd-L complex (**1**), one can observe three endothermic mass loss stages at 250, 409, and 467 °C. The 1st and 2nd decomposition steps are accompanied by a mass loss, 53.34% (calcd. 53.83%) due to the degradation of one ligand molecule. The 3rd stage involves a 17.35% mass loss, owing to the releasing of chlorine gas (calcd. 16.90%) leaving palladium oxide as a final residue at 507 °C.

The TGA/DTA curves of Pd-L (X = Br) complex (**2**) (Fig. 4a) exhibit five decomposition steps maximized at 296, 379, 426, 506 and 800 °C. The 1st and 2nd pronounced peaks are accompanied by a mass loss amounting to 22.19% (calcd. 21.99%) due to the removal of one bromine atom and two coordinated water molecules. The 3rd and 4th decomposition stages involve the loss of another bromine atom and benzimidazole ring. The final stage is attributed to the removal of N-methylene aniline with overall mass loss amounting to 76.78% (calcd. 77.44%), leaving Pd metal as a final residue at 1000 °C. On the other hand, the thermogram of Pd-L (X = I) complex (**3**) resembles complex (**2**) with four decomposition stages at 285, 419, 538 and 803 °C.

For Pd-L (X = SCN) complex (**4**), the degradation starts at 100 °C with three decomposition stages centered at 261, 411 and 800 °C (Fig. 4b). The first degradation step is due to the releasing of two SCN, two coordinated water molecules and one hydrated molecule. The 2nd and 3rd decomposition stages are attributed to the degradation of one ligand molecule leaving Pd metal as a final residue with overall mass loss amounting to 78.80% (calcd. 78.76%).

The first event in the Pd-L (X = NO_3) complex (**5**) is a composite one, which has three mutually endothermic overlapping peaks, maximized at 51, 140 and 295 °C owing to the elimi-

Table 2
Kinetic parameters, (E^*, ΔH^*, ΔG^*, kJ/mol), A (s^{-1}) and ΔS^* (J/K mol); determined using Coats–Redfern method and Horowitz–Metzger methods of the metal complexes under study.

Compound	Decomp. range	Coats–Redfern					Horowitz–Metzger				
		E^*	A	ΔS^*	ΔH^*	ΔG^*	E^*	A	ΔS^*	ΔH^*	ΔG^*
$[PdLCl_2]\cdot H_2O$	30–310	89	2×10^6	−124	86	129	111	7×10^6	−96	111	144
	310–420	44	2×10^5	−151	39	141	78	2×10^9	−72	78	127
	420–507	128	5×10^5	−143	122	228	143	2×10^6	−131	144	240
$[PdL(H_2O)_2]\cdot 2Br$	214–312	105	4×10^5	−143	100	182	122	3×10^6	−126	123	194
	312–390	57	2×10^5	−151	52	149	70	3×10^6	−126	71	153
	390–440	104	2×10^5	−151	98	204	113	1×10^5	−142	114	213
	440–600	169	2×10^6	−132	163	265	181	5×10^6	−124	182	278
	600–855	224	2×10^6	−137	215	362	224	2×10^6	−135	225	369
$[PdL(H_2O)_2]\cdot 2I$	200–310	158	5×10^6	−121	153	220	194	2×10^8	−93	194	246
	310–435	14	1×10^5	−151	9	113	26	2×10^9	−74	26	77
	435–555	358	5×10^8	−87	351	422	381	2×10^9	−76	381	443
	772–831	368	3×10^7	−111	360	479	389	8×10^7	−104	389	502
$[PdL(H_2O)_2]\cdot 2SCN\cdot H_2O$	225–360	170	2×10^7	−112	166	226	176	4×10^7	−105	176	232
	360–1000	230	4×10^7	−106	225	298	235	6×10^7	−103	235	306
$[PdL(H_2O)_2]\cdot 2NO_3$	30–91	20	2×10^5	−146	17	65	21	1×10^5	−139	22	67
	91–215	32	1×10^5	−149	29	90	33	1×10^5	−149	34	95
	215–350	55	1×10^5	−150	51	136	65	1×10^5	−137	66	144
	350–512	176	5×10^6	−123	171	255	180	7×10^6	−121	181	263
	725–862	291	7×10^6	−125	282	417	304	1×10^7	−119	304	433
$[PtLCl_2]$	170–400	27	2×10^5	−149	22	113	38	3×10^7	−108	38	105
	400–480	448	8×10^7	−46	442	475	447	8×10^7	−101	447	521

nation of two-coordinated water molecules, two molecules of nitrogen dioxide and oxygen gas. The 4th and 5th thermal stages, centered at 409 and 808 °C, are due to the degradation of one ligand molecule with overall mass loss amounting to 75.68% (calcd. 75.87%) leaving Pd metal as a final residue [28].

The TGA/DTA curves (Fig. 4c) of the platinum complex (**6**) reveal that the decomposition process proceeds *via* two main endothermic stages. The 1st step at 341 °C, is responsible for the elimination of benzimidazole ring with mass losses 23.42% (calcd. 24.13%). The 2nd event is a composite one with two mutually overlapping peaks at 420 and 455 °C. The mass loss for the 2nd event amounts to 36.30% (calcd. 35.99%). The thermal decomposition proceeds with the formation of Pt as residue.

The kinetics parameters are calculated by using Coats–Redfern [29] and Horowitz–Metzger methods [30]. According to the obtained data (Table 2), some complexes have negative entropy. This indicates that the complexes are formed spontaneously and are highly ordered in their activated states. In Pd-L (X = NO_3) complex (**5**), the values of activation energy increase on going from one thermal stage to another for a given complex, indicating that the rate of decomposition decreases in the same order. While, the values of the free activation energy ΔG^* increase significantly for the subsequent decomposition stages of a given complex. This is due to increasing the values of $T\Delta S^*$ significantly from one-step to another, which override the values of ΔH^*. This may be attributed to the structural rigidity of the remaining complex after the expulsion of one of the coordinated anions or water molecules, as compared with the precedent complex, which require more energy, $T\Delta S^*$ for its rearrangement before undergoing any compositional change. The positive ΔH^* values mean that the decomposition processes are endothermic.

3.6. X-ray powder diffraction

The X-ray powder diffraction patterns of the benzimidazole L, Pd-L (X = Cl) (**1**), Pd-L (X = Br) (**2**) and Pt-L (**6**) complexes were recorded over 2θ = 5–60° in order to obtain an idea about the lattice dynamics of these compounds. The values of 2θ, interplanar spacing d (Å) and the relative intensities (I/I°) of benzimidazole L and its complexes were tabulated in Table 3. The comparison between the obtained XRD patterns of L and its complexes (Fig. 5), throws light on the fact that each complex represents a definite compound with a distinct structure. This identification of the complexes was done by the known method [31]. Such facts suggest that the metal complexes are amorphous. The X-ray powder diffraction pattern of benzimidazole (L) shows a degree of crystallinity as the parent benzimidazole [32] with three low-angle diffraction peaks (below 11.00°) that are not observed in the benzimidazole. Several peaks characterized to the benzimidazole moiety are also observed at 18.18°, 34.09°, 37.59°, and 40.12°.

3.7. Theoretical calculations

3.7.1. Geometry optimization

Full geometry optimizations were performed at the DFT level of theory [9]. The optimized N15C7 and N16C7 bond lengths in the ligand L are 1.310 and 1.377 Å (Table 4) as calculated by the 6-31G(d) basis set. This confirms that the hydrogen atom is fixed at one of the two nitrogen atoms through the intermolecular hydrogen bonding. The benzimidazole L shows accumulation of the negative charge density on the pyridine-type nitrogen, which is a very important structural feature related directly to the ability to bind the metal ions. Several calculated thermodynamic parameters are also presented in Table 4.

The fully optimized geometries of cis-$PdLCl_2$ and cis-$PtLCl_2$ and numbering of atoms are shown in Fig. 6 and their geometric parameters are listed in Table 5. The coordination sphere around the metallic center in cis-$PdLCl_2$ and cis-$PtLCl_2$ complexes is made up of N_{py}, NH_{sec} and 2Cl completing the square planar geometry. The four donor atoms are coplanar, while the phenyl ring is bent out of the coordination plane by angle 112.765° (cis-$PdLCl_2$) and 118.532° (cis-$PtLCl_2$). It was found that the M-NH_{sec} (M = Pd or Pt) bond length is about 4.43% longer than the M-N_{py} bond distance [33]. In addition, the optimized Pd-NH_{sec} (2.167 Å) and Pd-N_{py} (2.071 Å) bond lengths are slightly longer

Table 3
X-ray diffraction data of benzimidazole L, Pd-L (X = Cl) and Pt-L complexes.

L			Pd-L (X = Cl) (**1**)			Pd-L (X = Br) (2)		
Angle (2θ)	d-Value (Å)	Relative intensity (I/I°) %	Angle (2θ)	d-Value (Å)	Relative intensity (I/I°) %	Angle (2θ)	d-Value (Å)	Relative intensity (I/I°) %
7.23	12.20	55.7	17.07	5.18	51.4	27.45	3.24	42.8
9.41	9.39	38.7	22.82	3.89	58.8	33.44	2.67	59.2
10.92	8.09	48.5	28.52	3.13	100.0	45.42	1.99	85.2
12.77	6.92	18.7	40.76	2.21	61.4	47.54	1.91	53.4
16.84	5.26	21.9	49.52	1.84	58.8	50.26	1.81	100.0
17.73	4.99	47.8				58.63	1.57	50.6
18.18	4.87	22.8						
18.91	4.69	36.2						
20.44	4.34	43.8						
21.03	4.22	32.7						
21.31	4.16	26.8						
21.93	4.04	23.8						
23.00	3.86	47.1						
23.600	3.76	55.7						
25.65	3.47	100.0						
26.56	3.35	33.3						
27.10	3.28	21.9						
28.01	3.18	18.7						
29.79	2.99	22.3						
30.59	2.92	25.2						
33.16	2.69	22.8						
34.09	2.63	12.1						
37.59	2.39	9.5						
40.12	2.24	4.0						

Table 4
Geometrical parameters optimized in L (bond length, and bond angle), theoretically computed energies, zero-point vibrational energies, rotational constants, entropies and dipole moment.

Bond lengths (Å)	B3LYP/6-31G(d)	B3LYP/LANL2DZ	Bond angles (°)	B3LYP/6-31G(d)	B3LYP/LANL2DZ
C1C2	1.409	1.421	C3C1C2	121.409	121.336
C1C3	1.392	1.404	C4C3C1	117.989	117.892
C3C4	1.399	1.407	C5C4C3	119.828	120.136
C4C5	1.415	1.428	C6C2C1	121.535	121.527
C2C6	1.393	1.406	C7N15C4	105.277	105.791
C4C7	2.147	2.187	C8C7N15	124.496	124.623
C7C8	1.502	1.506	N17C8C7	109.274	109.274
C8C9	2.473	2.504	C9N17C8	121.608	121.608
C9C10	1.410	1.422	C11C10C9	120.677	120.591
C10C11	1.390	1.401	C12C11C10	120.814	120.886
C11C12	1.399	1.412	C13C12C11	118.782	118.739
C12C13	1.394	1.407	C14C13C12	121.045	121.064
C13C14	1.396	1.407	N15C4C5	110.158	109.691
N15C7	1.310	1.330	N16C7N15	112.999	112.279
N16C7	1.377	1.394	N16C5C4	104.425	104.807
N17C9	1.389	1.390	H18C3C1	121.717	121.679
H18C3	1.086	1.086	H19C1C3	119.513	119.586
H19C1	1.086	1.087	H20C2C1	119.302	119.175
H20C2	1.086	1.087	H21C6C2	121.314	121.019
H21C6	1.086	1.087	H22N16C7	126.230	126.061
H22N16	1.009	1.011	H23C8C7	109.407	109.293
H23C8	1.102	1.106	H24C8C7	109.0856	109.318
H24C8	1.107	1.106	H25N17C9	116.544	120.764
H25N17	1.014	1.015	H26C10C9	119.124	119.254
H26C10	1.088	1.089	H27C11C10	119.147	119.223
H27C11	1.087	1.088	H28C12C11	120.577	120.585
H28C12	1.086	1.087	H29C13C12	119.997	119.850
H29C13	1.087	1.088	H30C14C13	119.385	119.243
H30C14	1.087	1.087			

	B3LYP/6-31G(d)	**B3LYP/LANL2DZ**
E (a.u.)	−705.585	−705.470
Zero-point *E* (kcal mol^{-1})	153.676	154.516
Rotational constants (GHz)	1.975, 0.179, 0.161	1.980, 0.170, 0.157
Entropy (cal mol^{-1} K^{-1})		
Translational	42.110	42.110
Rotational	33.033	33.079
Vibrational	42.783	41.750
Total dipole moment (D)	3.615	4.312

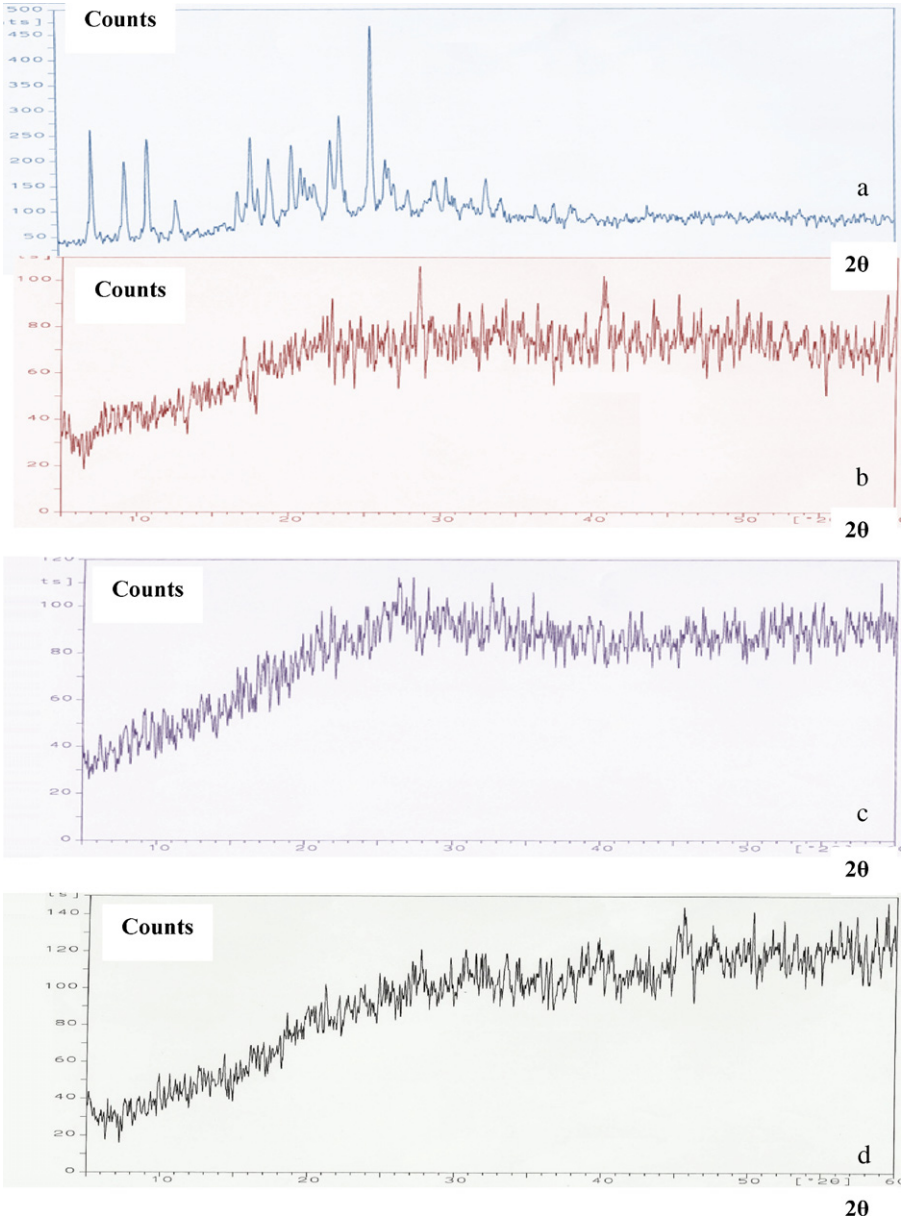

Fig. 5. X-ray diffraction pattern of (a) benzimidazole L, (b) Pd-L (X = Cl), (c) Pd-L (X = Br), (d) Pt-L complexes.

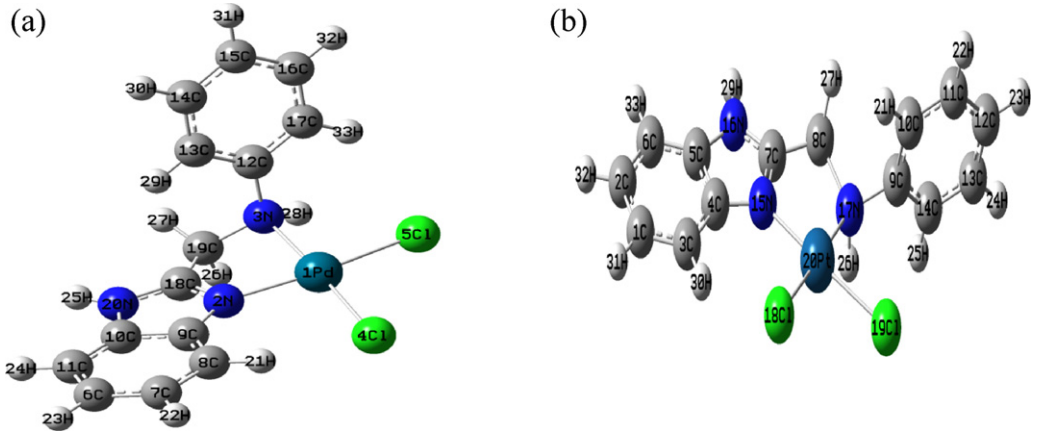

Fig. 6. Optimized structures of (a) cis-$PdLCl_2$ complex, (b) cis-$PtLCl_2$ complexes.

Table 5
Selected bond lengths (Å), angles (°) and charge for cis-$PdLCl_2$ and cis-$PtLCl_2$ complexes.

cis-$PdLCl_2$					cis-$PtLCl_2$				
Bond lengths (Å)		Bond angles (°)		Charge	Bond lengths (Å)		Bond angles (°)		Charge
C6C7	1.422	C6C7C8	121.733	Pd = 0.687	C1C2	1.421	C1C2C6	121.488	Pt = 0.619
C7C8	1.402	C7C8C9	116.990	N2 = −0.603	C1C3	1.402	C2C6C5	116.525	N15 = −0.561
C8C9	1.406	C8C9C10	121.013	N3 = −0.691	C3C4	1.407	C6C5C4	122.322	N17 = −0.697
C9C10	1.425	C9C10C11	122.121	Cl4 = −0.505	C4C5	1.425	C5C4C3	120.731	Cl18 = −0.496
C10C11	1.404	C6C11C10	116.487	Cl5 = −0.549	C5C6	1.404	C4C3C1	117.086	Cl19 = −0.515
C6C11	1.404	C7C6C11	121.655	C6 = −0.213	C2C6	1.404	C3C1C2	121.847	C1 = 0.153
C10N20	1.410	C10N20C18	107.673	C7 = −0.198	C7C8	1.496	C5N17C7	107.690	C2 = 0.149
C9N2	1.409	C9N2C18	107.548	C8 = −0.251	C9C10	1.405	C4N15C7	107.332	C3 = −0.186
C18N20	1.378	N2C18N20	111.184	C9 = 0.151	C10C11	1.404	N15C7N16	111.345	C4 = −0.214
C18N2	1.337	C18C19N3	108.461	C10 = 0.149	C11C12	1.410	C7C8N17	108.907	C5 = −0.198
C18C19	1.505	C19N3C12	116.787	C11 = −0.187	C12C13	1.407	N15PtN17	81.207	C6 = −0.251
C19N3	1.502	C12C13C14	119.613	C12 = 0.163	C13C14	1.408	Cl18PtC19	90.479	C7 = 0.472
C12N3	1.467	C12N3Pd	112.765	C13 = −0.225	C9C14	1.403	N17C9C14	119.301	C8 = −0.244
C12C13	1.409	C13C14C15	120.492	C14 = −0.189	N15C7	1.338	N17C9C10	119.658	C9 = 0.164
C13C14	1.407	C14C15C16	119.462	C15 = −0.216	N16C7	1.376	C9C10C11	119.195	C10 = −0.241
C14C15	1.406	C15C16C17	120.568	C16 = −0.194	N17C9	1.480	C10C11C12	120.400	C11 = −0.197
C15C16	1.409	C13C12C17	120.278	C17 = −0.261	N15C4	1.415	C11C12C13	119.855	C12 = −0.207
C16C17	1.404	Cl4PdC15	95.065	C18 = 0.473	N16C5	1.408	C12C13C14	120.025	C13 = −0.188
C12C17	1.410	N2PdN3	80.673	C19 = −0.252	N17C8	1.522	C13C14C9	119.490	C14 = −0.233
N2Pd	2.071				Pt20Cl18	2.368	C10C9C14	121.026	N16 = −0.599
N3Pd	2.167				Pt20Cl19	2.386	C9N17Pt	118.532	
Cl4Pd	2.369				N15Pt20	2.071			
Cl5Pd	2.387				N17Pt20	2.168			

E (a.u.)	−862.220	−854.633
Zero-point *E* (kcal mol^{-1})	158.382	158.387
Rotational constants (GHz)	0.325, 0.195, 0.142	0.430, 0.158, 0.122
Entropy (cal mol^{-1} K^{-1})		
Translational	43.843	44.443
Rotational	34.837	34.920
Vibrational	62.814	64.332
Total dipole moment (*D*)	14.915	15.445

than the Pt-NH_3 bond distance in cis-platin by 0.16 and 0.06 Å, respectively, and are in agreement with that observed in some benzimidazole complexes [34]. However, the Pd–Cl bonds are longer than Pt–Cl bond by 0.06 and 0.03 Å for Pd–Cl5 and Pd–Cl4, respectively, owing to the difference in sizes between the metals.

The optimized N2-Pd-N3 (80.673°) is smaller than NH_3-Pt-NH_3 in cis-platin by 6.327° and this can be interpreted in terms of CH_2 group, which connects the two coordination sites (N2 and N3) and prevent the opening of this angle. In addition, the calculated Cl4–Pd–Cl5 (95.065°) angle is larger than the experimental one in cis-platin by 3.165° [35], since the intramolecular hydrogen bonding N3–H28···Cl5 (2.721 Å) opens up Cl4–Pd–Cl5 angle. The optimized N15PtN17 bond angle in the cis-$PtLCl_2$ complex is close to that found in cis-$PdLCl_2$ complex, while the Cl18PtC19 is slight different from that exists in cis-platin by 1.5°. This indicates that there is weak or no intramolecular hydrogen bonding as found in the cis-$PdLCl_2$ complex and this may be attributed to the significant difference in the bending angle of aniline ring as previously mentioned. In addition, both C12N3 and C19N3 bond lengths in cis-$PdLCl_2$ complex were increased upon the coordination of secondary amino group N3H to the metal center.

3.7.2. Natural bond orbital (NBO) analysis

The natural bond orbital (NBO) analysis of cis-$PdLCl_2$ complex was performed. The NBO analysis can be used to estimate the delocalization of electron density between occupied Lewis-type orbitals and formally unoccupied non-Lewis NBOs (antibonding or Rydberg), which corresponds to a stabilizing donor–acceptor interaction [36]. Table 5 collects the natural charges on atoms. The largest negative charges are located on the two nitrogen atoms, N_{py} (−0.603e) and NH_{sec} (−0.691e). According to the NBO results, the electron configuration of Pd is: [core]$5s^{0.35}4d^{8.93}5p^{0.02}5d^{0.01}6p^{0.01}$. Thus, 36 core electrons, 9.28 valence electrons (on 5s and 4d atomic orbitals) and 0.04 Rydberg electrons (mainly on 5p, 5d, and 6p orbitals) give the 45.31 electrons. This is consistent with the calculated natural charge on Pd atom (+0.687) in cis-$PdLCl_2$, which corresponds to the difference between 45.31e and the total number of electrons in the isolated Pd atom (46e). In addition, the two chlorine atoms (Cl4 and Cl5) have larger negative charge −0.505e and −0.549e, respectively. Thus, the positive atomic charge upon the Pd(II) was substantially reduced as a consequence of electron density donation from the pyridine like nitrogen, secondary amino group and two chlorine atoms. Table 6 lists the calculated occupancies of natural orbitals. Three classes of NBOs are included, the Lewis-type (s and p bonding or lone pair) orbitals, the valence non-Lewis (acceptors, formally unfilled) orbitals and the Rydberg NBOs, which originate from orbitals outside the atomic valence shell. The calculated natural hybrids on atoms are also given in this table. According to calculations, the palladium atom forms two sigma bonds with two chlorine atoms, while the two bonds between palladium and the nitrogen atoms can be described as donation of electron density from a lone pair (LP) orbital on each nitrogen atom to palladium molecular orbitals. As follows from Table 6, the σ(Pd–Cl4) bond is formed from an $sp^{0.01}d^{1.04}$ hybrid on palladium atom (which is a mixture of 48.80% s, 0.53% p and 50.67% d atomic orbitals) and $sp^{14.77}$ hybrid on the chlorine atom (93.66% p contribution). Thus, the σ(Pd–Cl4) bond is strongly polarized towards the chlorine atom, with about 76.80% of electron density concentrated on the chlorine atom. The strength of this interaction can be estimated by the second order perturbation theory.

Table 7 lists the selected values of the calculated second order interaction energy (E^2) between donor–acceptor orbitals in cis-$PdLCl_2$. The strongest interactions are the electron donations from a lone pair orbital on the nitrogen atoms, LP(1)N2 to the antibonding acceptor σ*(Pd–Cl5) orbitals, e.g. LP(1)N2 → σ*(Pd–Cl5). As shown in Table 6, the LP(1)N2 orbital has 69.35% p-character and is occu-

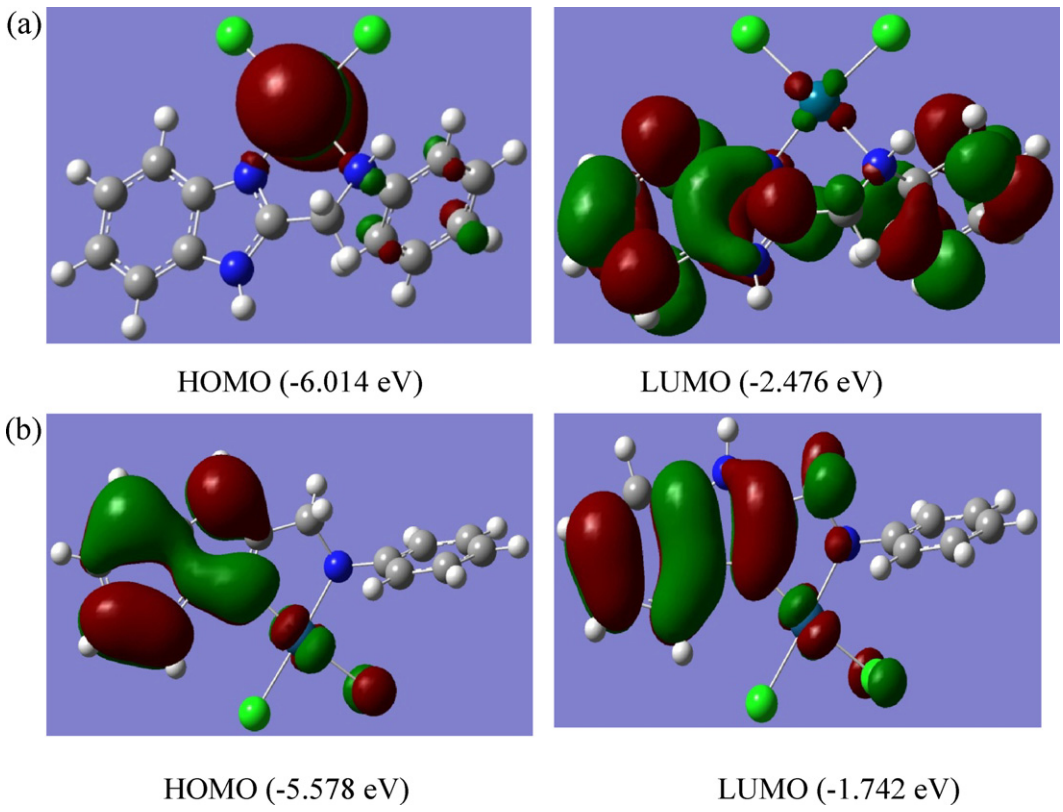

Fig. 7. Molecular orbital surfaces and energy levels of (a) cis-$PdLCl_2$ complex, (b) cis-$PtLCl_2$ complexes.

Table 6
Occupancy of natural orbitals (NBOs) and hybrids calculated for cis-$PdLCl_2$ complex.

Donor[a] Lewis-type NBOs (A-B)	Occupancy	Hybrid[b]	AO (%)[c]	Acceptor[d] non Lewis NBOs	NBOs
σ(C18-N2)	1.983	$sp^{1.84}$ (N2) $sp^{2.23}$ (C18)	s(35.23)p(64.77) s(30.92)p(69.08)	σ*(C18-N2)	0.036
σ(C12-N3)	1.985	$sp^{1.98}$ (N3) $sp^{2.83}$ (C12)	s(35.23)p(64.77) s(26.09)p(73.91)	σ*(C12-N3)	0.040
σ(C19-N3)	1.980	$sp^{2.60}$ (N3) $sp^{3.40}$ (C19)	s(27.78)p(72.22) s(22.73)p(77.27)	σ*(C19-N3)	0.023
σ(Pd–Cl4)	1.933	$sp^{0.01}d^{1.04}$ (Pd) $sp^{14.77}$ (C14)	s(48.80)p(0.53)d(50.67) s(6.34)p(93.66)	σ*(Pd–Cl4)	0.322
σ(Pd–Cl5)	1.937	$sp^{0.01}d^{1.09}$ (Pd) $sp^{13.32}$ (C15)	s(47.55)p(0.49)d(51.95) s(6.99)p(93.01)	σ*(Pd–Cl5)	0.284
σ(N3-H28)	1.981	$sp^{2.99}$ (N3)	s(25.08)p(74.92)	RY*(1)N2	0.004
LP(1)N2	1.730	$sp^{2.26}$	s(0.02)p(99.98)	RY*(1)N3	0.007
LP(1)N3	1.713	$sp^{6.37}$	s(13.57)p(86.43)	RY*(1)Cl4	0.0003
LP(1)Cl4	1.990	$sp^{0.26}$	s(79.62)p(20.38)	RY*(1)Cl5	0.0004
LP(1)Cl5	1.990	$sp^{0.41}$	s(71.11)p(28.89)	RY*(1)Pd	0.018
LP(1)Pd	1.995	$sp^{0.58}d^{99.99}$	s(0.11)p(0.07)d(99.82)	RY*(2)Pd	0.003
LP(2)Pd	1.991	$sp^{0.01}d^{39.43}$	s(2.47)p(0.01)d(97.51)	RY*(3)Pd	0.0025
LP(3)Pd	1.990	$sp^{4.32}d^{99.99}$	s(0.02)p(0.08)d(99.90)		

[a] LP(n)A is a valence lone pair orbital (n) on A atom.
[b] Hybrid on A atom in the A–B bond or otherwise, as indicated.
[c] Percentage contribution of atomic orbitals in NBO hybrid.
[d] Asterisk (*) denotes antibonding, and Ry corresponds to the Rydberg NBO orbital.

Table 7
Second-order interaction energy (E^2, kcal mol^{-1}) between donor and acceptor orbitals in cis-$PdLCl_2$ complex calculated at B3LYP/LANL2DZ level of theory (selected).

Donor → acceptor	E^2	Donor → acceptor	E^2
LP(1)N2 → σ*(Pd–Cl5)	66.23	LP(1)Cl4 → σ*(Pd–Cl4)	13.11
LP(1)N3 → σ*(Pd–Cl4)	50.5	σ(N20-C18) → σ*(Pd–Cl4)	3.55
σ(Pd–Cl4) → σ*(Pd–Cl5)	10.13		

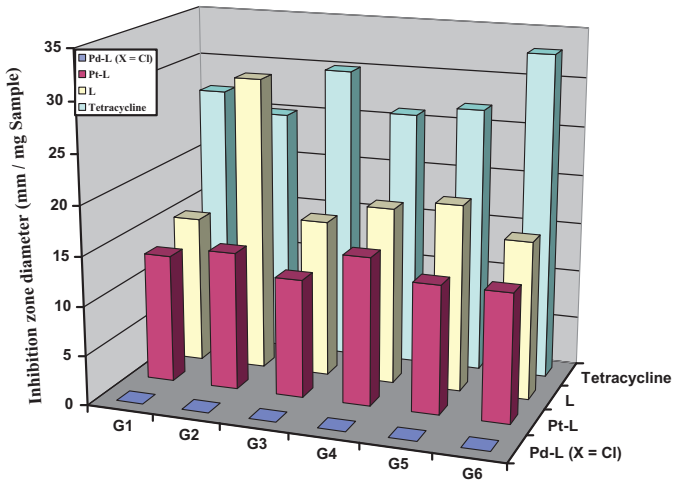

Fig. 8. Antibacterial activities of benzimidazole L and its complexes; Pd-L (X = Cl) (**1**) and Pt-L (**6**) against *B. subtilis* (G1), *S. aureus* (G2), *S. faecalis* (G3) as Gram-positive, (G4) *P. aeruginosa* (G4), *E. coli* (G5), *N. gonorrhoeae* (G6) as Gram-negative bacteria.

pied by 1.731 electrons (this is consistent with a delocalization of electron density from the idealized occupancy of 2.0e). The donation of electron density from the coordination sites in the ligand to the Pd molecular orbitals has a clear correspondence to a chemical picture of the coordination bonds.

3.7.3. Frontier molecular orbitals

The frontier molecular orbitals play an important role in the electric and optical properties [37]. Fig. 7 shows the distributions and energy levels of the HOMO, and LUMO orbitals computed at the B3LYP/LANL2DZ level for cis-$PdLCl_2$ and cis-$PtLCl_2$ complexes. The value of the energy separation between the HOMO and LUMO is 0.130 and 0.141 eV for cis-$PdLCl_2$ and cis-$PtLCl_2$, respectively.

3.8. Structural interpretation

The structures of the Pd(II) (X = Cl, Br, I, SCN and NO_3) and Pt(II) (X = Cl) complexes are elucidated by the elemental analyses, FT-IR, ^{1}H NMR, MS, UV/vis, thermal analysis (TGA/DTA) and molar conductance data. From IR and ^{1}H NMR data, it is concluded that the benzimidazole L behaves as a neutral ligand with NNH sites coordinating to the metal ions *via* the pyridine-type nitrogen (N_{py}) of the benzimidazole ring and the secondary amino group (NH_{sec}). From the molar conductance data of the complexes, it was found that the Pd(II) (X = Cl) and Pt(II) complexes are non-electrolytes, while the Pd(II) complexes (X = Br, I, SCN or NO_3) are ionic. Based on the above observations, square planar geometry is suggested for the investigated complexes with the general formula; $[MLCl_2]\cdot zH_2O$ (M = Pd, $z = 0$; M = Pt, $z = 1$) and $[PdL(OH_2)_2]\cdot 2X\cdot zH_2O$ (X = Br, I, NO_3, $z = 0$; X = SCN, $z = 1$).

3.9. Biological activity

3.9.1. Antimicrobial activity

The data showed that the ligand L and its Pt-L complex (**6**) have the capacity of inhibiting the metabolic growth of the investigated bacteria; *B. subtilis*, *S. aureus*, *S. faecalis* as Gram-positive bacteria and *E. coli*, *P. aeruginosa*, *N. gonorrhoeae* as Gram-negative bacteria; to different extents as shown in Fig. 8. The size of the inhibition zone depends upon the culture medium, incubation conditions, rate of diffusion and the concentration of the antibacterial agent (the activity increases as the concentration increases).

The benzimidazole L is active against both types of the bacteria, which may indicate broad-spectrum properties. The remarkable activity of this compound may be arising from the benzimidazole ring, which may play an important role in the antibacterial activity. The mode of action may involve the formation of a hydrogen bond through the pyridine-type nitrogen of the imidazole ring with the active centers of the cell constituents, resulting in interference with the normal cell process. The benzimidazole L is more toxic against Gram-positive than Gram-negative bacteria that is related to the cell wall structure of the bacteria. It is important to point out that the benzimidazole L is more toxic against the bacterium *S. aureus* with a minimum inhibitory concentration (58 μg/mL) as compared with the standard tetracycline (82 μg/mL).

However, the Pd-L complex (**1**) was inactive against all the test organisms, while the platinum complex (**6**) possesses lower activity than that of the ligand itself as shown in Fig. 8. A possible explanation for the poor activity of these complexes may be attributed to their inability to chelate metals essential for the metabolism of microorganisms and/or to form hydrogen bonds with the active centers of cell structures, resulting in an interference with the normal cell cycle. Furthermore, the low activity of these complexes may be also due to their low lipophilicity, because of which penetration of the complex through the lipid membrane was decreased and hence, they could neither block nor inhibit the growth of the microorganism. Therefore, the toxicity of the complexes can be related to strength of the M–L bonds, besides other factors such as size of the cation, receptor sites, diffusion, and a combined effect of the metal and the ligands for inactivation of the bio-molecules.

3.9.2. Cytotoxicity

To evaluate the potential usefulness of the studied complexes synthesized as antitumor agents, three cell lines of different origin; *breast cancer* (MCF-7), *Colon Carcinoma* (HCT) and *human hepatocellular Carcinoma* (Hep-G2) were treated. This experiment was performed at 100 μM and compared with cis-platin. These complexes showed activity against the studied cell lines. The IC_{50} (the concentration that inhibited in 50% of the cellular proliferation) of these compounds and cis-platin were determined. According to Shier [38], the compounds exhibited IC_{50} activity in the range 10–25 μg/mL are considered weak anticancer drugs, while those of IC_{50} between 5.00 and 10.00 μg/mL are moderate and compounds of activity below 5.00 μg/mL are considered strong agents.

It was found that the Pd-L (**1**) and Pt-L (**6**) complexes have moderate toxicity against Hep-G2 cells (according to Shier scale). The palladium complex has IC_{50} value of 15 μM (equivalent to 6.27 μg/mL) as compared with the IC_{50} of cis-platin; 11.9 μM (equivalent to 3.57 μg/mL). In addition, the Pd-L (**1**) is more toxic than Pt-L (**6**) complex. This happens because the ligand-exchange behavior of platinum compounds is quite slow, i.e. inert complexes, which gives them a high kinetic stability and results in ligand-exchange reactions of minutes to days, rather than microseconds to seconds for many other coordination compounds. In addition, another unusual phenomenon deals with the preferred ligands for platinum ions is that Pt(II) has a strong thermodynamic preference for binding to S-donor ligands and for this reason, one would predict that platinum compounds would perhaps never reach DNA, with many cellular platinophiles (S-donor ligands, such as glutathione, methionine) as competing ligands in the cytosol [39].

The Pt-L complex (IC_{50} = 14.7 μM; 7.19 μg/mL) shows moderate cytotoxicity against HCT cells as compared with cis-platin (IC_{50} = 10.9 μM; 3.27 μg/mL). For MCF-7 cells, the Pt-L complex has also moderate antitumor activity with IC_{50} = 12.4 μM; equivalent to 6.06 μg/mL, while the IC_{50} of cis-platin is 9.91 μM (equivalent to 2.97, μg/mL).

4. Conclusion

Better approaches to the synthesis of the benzimidazole L and its complexes were developed. On the basis of agreement between the calculated and experimental results, assignments of all the fundamental vibrational modes of benzimidazole L and its complexes were examined and proposed at higher level of theory. The inclusion of solvation to the ^{1}H NMR calculations is necessary especially for acidic protons in order to obtain accurate values. The equilibrium geometries, and harmonic frequencies, of the metal complexes were determined and analyzed at DFT level of theory utilizing LANL2DZ basis set. NBO analysis reveals that the strong coordination bonds result from donation of electron density from a lone pair orbital on the nitrogen atoms to the acceptor metal molecular orbitals, e.g. (LP(1)N2 → σ*(Pt–Cl5)) and (LP(1)N3 → σ*(Pt–Cl4)). The studied ligand is more toxic against the bacterium *S. aureus* with MIC (58 μg/mL) than the standard tetracycline (82 μg/mL). The complexes show moderated cytotoxicity against the investigated cell lines and represent an interesting class of new compounds from the viewpoint of their physicochemical and structural.

Acknowledgments

We would like to extend our grateful thanks to Dr. Mohamed Elshakre, Chemistry Department, Faculty of Science, Cairo University for allowing us to use his version of the *GAUSSIAN 03* package of programs. Deep thanks to Prof. Dr. Samia Showman, professor of Medical Biochemistry, National Cancer Centre, Cairo University, for the great helps and support during the biological part.

References

[1] (a) B.K. Keppler, Metal Complexes in Cancer Chemotherapy, VCH, Weinheim, 1993;
(b) G. Berthon, Handbook of Metal Ligand Interactions in Biological Fluids, Marcel Dekker, New York, 1995.
[2] (a) K. Akdi, R.A. Vilaplana, S. Kamah, J.A.R. Navarro, J.M. Salas, F. González-Vílcheza, J. Inorg. Biochem. 90 (2002) 51;
(b) A. Matilla, J.M. Tercero, N.H. Dung, B. Voissat, J.M. Pérez, C. Alonso, D. Martín-Ramos, J. Niclós-Gutiérrez, J. Inorg. Biochem. 55 (1994) 235.
[3] (a) F. Gumus, G. Eren, L. Acik, A. Celebi, F. Ozturk, R. Ilikci Sagkan, S. Gur, A. Ozkul, A. Elmali, Y. Elerman, J. Med. Chem. 52 (5) (2009) 1345–1357;
(b) M. Goekce, S. Utku, S. Guer, A. Oezkul, F. Gumus, Eur. J. Med. Chem. 40 (2) (2005) 135–141;
(c) F. Gumus, O. Algul, G. Eren, H. Eroglu, N. Diril, S. Gur, A. Ozkul, Eur. J. Med. Chem. 38 (5) (2003) 473–480;
(d) F. Gumus, A.B. Demirci, T. Oezden, H. Eroglu, N. Diril, Pharmazie 58 (5) (2003) 303–307;
(e) F. Gumus, I. Pamuk, T. Oezden, S. Yildiz, N. Diril, E. Oksuzoglu, S. Gur, A. Ozkul, J. Inorg. Biochem. 94 (3) (2003) 255–262.
[4] (a) V. Rajendiran, M. Murali, E. Suresh, S. Sinha, K. Somasundaram, M. Palaniandavar, Dalton Trans. (2008) 148;
(b) J. Mann, A. Baron, Y. Opoku-Boahen, E. Johansson, G. Parkinson, L.R. Kelland, S. Neidle, J. Med. Chem. 44 (2001) 138.
[5] (a) E. Bouwmann, W.L. Driessen, J. Reedijk, Coord. Chem. Rev. 104 (1990) 143;
(b) M.A. Puja, T.D. Bharamgouda, N.D. Sathyanarayna, Trans. Met. Chem. 13 (1988) 423.
[6] M. Boča, R.F. Jameson, W. Linert, Coord. Chem. Rev. 255 (2011) 290–317.
[7] N.T. Abdel-Ghani, A.M. Mansour, J. Mol. Struct. 991 (2011) 108–126.
[8] A. Skoog, D.M. West, Fundamentals of Analytical Chemistry, Thomson, Brooks, Cole, New York, 2004.
[9] A.D. Becke, J. Chem. Phys. 98 (1993) 5648.
[10] M.J. Frisch, G.W. Trucks, H.B. Schlegel, G.E. Scuseria, M.A. Robb, J.R. Cheeseman, V.G. Zakrzewski, J.A. Montgomery, R.E. Stratmann, J.C. Burant, S. Dapprich, J.M. Millam, A.D. Daniels, K.N. Kudin, M.C. Strain, O. Farkas, J. Tomasi, V. Barone, M. Cossi, R. Cammi, B. Mennucci, C. Pomelli, C. Adamo, S. Clifford, J. Ochterski, G.A. Petersson, P.Y. Ayala, Q. Cui, K. Morokuma, D.K. Malick, A.D. Rabuck, K. Raghavachari, J.B. Foresman, J. Cioslowski, J.V. Ortiz, A.G. Baboul, B.B. Stefanov, G. Liu, A. Liashenko, P. Piskorz, I. Komaromi, R. Gomperts, R.L. Martin, D.J. Fox, T. Keith, M.A. Al-Laham, C.Y. Peng, A. Nanayakkara, C. Gonzalez, M. Challacombe, P.M.W. Gill, B.G. Johnson, W. Chen, M.W. Wong, J.L. Andres, M. Head-Gordon, E.S. Replogle, J.A. Pople, GAUSSIAN 03 (Revision A.9), Gaussian, Inc., Pittsburgh, 2003.
[11] A. Frisch, A.B. Nielson, A.J. Holder, GAUSSVIEW User Manual, Gaussian Inc., Pittsburgh, PA, 2000.
[12] R. Ditchfield, Chem. Phys. 76 (1972) 5688.
[13] (a) D. Greenwood, Antimicrobial Chemotherapy, Bailliere, Tindall, London. Part II. Laboratory Aspects of Antimicrobial Therapy, 1983, p. 71;
(b) V. Lorian, Antibiotics in Laboratory Medicine, Williams & Wilkins, Baltimore, 1996.
[14] National Committee for Clinical Laboratory Standards, NCCLS Approval Standard Document M2-A7, Vilanova, PA, 2000.
[15] C.M. Lozano, O. Cox, M.M. Muir, J.D. Morales, J.L. Rodríguez-Cabáin, P.E. Vivas-Mejfa, F.A. Gonzalez, Inorg. Chim. Acta 271 (1998) 137–144.
[16] (a) P. Skehan, R. Smreng, D. Scudiero, A. Monks, J. McMahon, D. Vistica, J.T. Warren, H. Bokesch, S. Kenney, M.R. Boyd, J. Natl. Cancer Inst. 82 (1990) 107–1112;
(b) A. Monks, D. Scudiero, P. Skehan, K. Paull, D. Vistica, C. Hose, J. Langley, P. Cronise, A. Viagro-Wolff, M. Gra-Goodrich, J. Natl. Cancer Inst. 83 (1991) 757–766.
[17] (a) G. Rauhut, P. Pulay, J. Phys. Chem. 99 (1995) 3093–3100;
(b) J.A. Pople, H.B. Schlegel, R. Krishnan, J.S. Defrees, J.S. Binkley, M.J. Frisch, R.A. Whiteside, Int. J. Quantum Chem.: Quantum Chem. Symp. 15 (1981) 269.
[18] (a) M.W. Ellzy, J.O. Jensen, H.F. Hameka, J.G. Kay, D. Zeroka, Spectrochim. Acta 57A (2001) 2417;
(b) J.O. Jensen, A. Banerjee, C.N. Merrow, D. Zeroka, J.M. Lochner, J. Mol. Struct.: Theochem. 531 (2000) 323;
(c) J.O. Jensen, D. Zeroka, J. Mol. Struct.: Theochem. 487 (1999) 267.
[19] O. Sala, N.S. Goncalves, L.K. Noda, J. Mol. Struct. 411 (2001) 565–566.
[20] K. Nakamoto, "Infrared and Raman Spectra of Inorganic and Coordination Compounds", Part B: Applications in Coordination, Organometallic, and Bioinorganic Chemistry, 6th ed., John Wiley & Sons Inc., New Jersey, 2009.
[21] W. Nawrocka, B. Sztuba, M.W. Kowalaka, H. Liszkiewicz, Farmaco 59 (2004) 83.
[22] (a) E. Bednarek, J.C. Dobrowolski, K. Dobrosz-Teperek, L. Kozerski, W. Lewandowski, A.P. Mazurek, J. Mol. Struct. 554 (2000) 233–243;
(b) F.S. Miranda, F.G. Menezes, J. Vicente, A.J. Bortoluzzi, C.Z. Ademir-Neves, N.S. Gonçalves, J. Mol. Struct. 938 (2009) 1–9.
[23] R.M. Issa, A.A. Hassanein, I.M. El-Mehasseb, R.I. Abed. El-Wadoud, Spectrochim. Acta Part A 65 (2006) 206–214.
[24] (a) M. Krishnamurthy, P. Phaniraj, S.K. Dogra, J. Chem. Soc. Perkin Trans. II (1986) 1917–1925;
(b) A.K. Mishra, S.K. Dogra, Bull. Chem. Soc. Jpn. 58 (1985) 3587; A.K. Mishra, S.K. Dogra, J. Photochem. 31 (1985) 333; A.K. Mishra, S.K. Dogra, Indian J. Phys. Sect. B 54 (1984) 480; A.K. Mishra, S.K. Dogra, Spectrochim. Acta. Part A 39 (1983) 609.
[25] R.M. Issa, S.A. El-Daly, N.A. El-Wakiel, Spectrochim. Acta Part A 59 (2003) 723–728.
[26] (a) A.B.P. Lever, Inorganic Electronic Spectroscopy, 2nd ed., Elsevier, Amsterdam, 1982, pp. 544–552;
(b) D.X. West, M.S. Lockwood, A. Liberta, X. Chen, R.D. Willet, Trans. Met. Chem. 18 (1993) 221.
[27] S.P. Perlepes, P. Jacobs, H.O. Desseyn, J.M. Tasangaris, Spectrochim. Acta 43A (1987) 771.

[28] N.T. Ghani, A.M. Mansour, Inorg. Chim. Acta 373 (2011) 249–258.
[29] A.W. Coats, J.P. Redfern, Nature 201 (1964) 68.
[30] H.H. Horowitz, G. Metzger, Anal. Chem. 85 (1963) 1464.
[31] B.D. Cullity, Elements of X-ray Diffraction, 2nd ed., Addison-Wesley Inc., 1993.
[32] N. Vijayan, R. Ramesh Babu, R. Gopalakrishnan, P. Ramasamy, W.T.A. Harrison, J. Cryst. Growth 262 (2004) 490–498.
[33] D.N. Neogi, P. Das, A.N. Biswas, P. Bandyopadhyay, Polyhedron 25 (2006) 2149.
[34] (a) R.W. Hay, T. Clifford, P. Lightfoot, Polyhedron 17 (20) (1998) 3575–3581; (b) X. Jing-Yuan, G. Wen, L. Ling, Y. Shi-Ping, C. Peng, L. Dai-Zheng, J. Zong-Hui, J. Mol. Struct. 644 (2003) 23–27.
[35] R. Wysokiński, D. Michalska, J. Comput. Chem. 22 (9) (2001) 901–912.
[36] A.E. Reed, L.A. Curtiuss, F. Weinhold, Chem. Rev. 88 (1988) 899.
[37] I. Fleming, Frontier Orbitals and Organic Chemical Reactions, Wiley, London, 1976.
[38] W.T. Shier, Mammalian Cell Culture on $5 a day: A Lab Manual of Low Cost Methods, University of the Philippines, Los Banos, 1991.
[39] M. Pérez-Cabré, G. Cervantes, V. Moreno, M.J. Prieto, J.M. Pérez, M. Font-Bardia, X. Solans, J. Inorg. Biochem. 98 (2004) 510–521.